



Constraints on the photon polarisation in $b \rightarrow s\gamma$ transitions using $B_s^0 \rightarrow \phi e^+ e^-$ decays

LHCb collaboration[†]

Abstract

An angular analysis of the $B_s^0 \rightarrow \phi e^+ e^-$ decay is performed using the proton-proton collision dataset collected between 2011 and 2018 by the LHCb experiment, corresponding to an integrated luminosity of 9 fb^{-1} at centre-of-mass energies of 7, 8 and 13 TeV. The analysis is performed in the very low dielectron invariant mass-squared region between 0.0009 and $0.2615 \text{ GeV}^2/c^4$. The longitudinal polarisation fraction of the ϕ meson is measured to be less than 11.5% at 90% confidence level. The $A_{\text{T}}^{\text{Re}CP}$ observable, which is related to the lepton forward-backward asymmetry, is measured to be $0.116 \pm 0.155 \pm 0.006$, where the first uncertainty is statistical and the second systematic. The transverse asymmetries, $A_{\text{T}}^{(2)}$ and $A_{\text{T}}^{\text{Im}CP}$, which are sensitive to the virtual photon polarisation, are found to be $-0.045 \pm 0.235 \pm 0.014$ and $0.002 \pm 0.247 \pm 0.016$, respectively. The results are consistent with Standard Model predictions.

Published in JHEP **03** (2025) 047

© 2025 CERN for the benefit of the LHCb collaboration. [CC BY 4.0 licence](#).

[†]Authors are listed at the end of this paper.

1 Introduction

In the Standard Model of particle physics (SM), processes involving $b \rightarrow s\gamma$ transitions are suppressed as they occur through flavour-changing neutral currents, mediated by loop processes involving electroweak penguin diagrams. The study of these processes provides insight into physics beyond the SM (BSM) due to potential deviations that may appear [1–6]. In the SM, the electroweak charged current has chiral interactions, coupling only to left-handed quarks. As a result, in $b \rightarrow s\gamma$ transitions, the photons are predominantly left-handed, with a small right-handed contribution that has a relative amplitude proportional to the ratio of the s - to b -quark masses. The presence of a significant right-handed polarisation would indicate a clear evidence of BSM physics.

The BaBar [7–9], Belle [10–13], Belle II [14] and LHCb [15, 16] collaborations have tested the photon polarisation in $b \rightarrow s\gamma$ transitions through measurements of the inclusive $B \rightarrow X_s\gamma$ branching fraction, CP asymmetries in radiative B^0 and B_s^0 decays, and by conducting an angular analysis of radiative A_b^0 decays. The strongest constraint to date comes from an angular analysis of $B^0 \rightarrow K^{*0}e^+e^-$ decays¹ by the LHCb experiment [17], isolating the dominant $b \rightarrow s\gamma$ contribution by restricting the dilepton invariant mass-squared, q^2 , to small values. The $b \rightarrow se^+e^-$ transition is particularly sensitive to the photon pole due to the smallness of the electron mass.

This paper presents the first angular analysis of the $B_s^0 \rightarrow \phi e^+e^-$ decay² in the very low q^2 region located between 0.0009 and 0.2615 GeV²/c⁴, chosen to be identical to the kinematical region of Ref. [17]. The ϕ meson is reconstructed via its $\phi \rightarrow K^+K^-$ decay. This analysis uses the data collected by the LHCb experiment between 2011 and 2018. The $B_s^0 \rightarrow \phi e^+e^-$ channel is experimentally cleaner than $B^0 \rightarrow K^{*0}e^+e^-$ as partially reconstructed background contributions from higher hadronic resonances are suppressed to a negligible level. In addition, the narrow width of the ϕ meson reduces sources of experimental backgrounds. Despite the lower production rate of B_s^0 mesons compared to B^0 mesons and the smaller branching fraction of the hadronic resonance for the B_s^0 channel, the analysis of the $B_s^0 \rightarrow \phi e^+e^-$ decay in the very low q^2 region provides valuable and complementary insights.

The $B_s^0 \rightarrow \phi e^+e^-$ decay is described across the entire q^2 spectrum by the left (right)-handed Wilson coefficients $C_7^{(\prime)}$, $C_9^{(\prime)}$, and $C_{10}^{(\prime)}$ [18, 19]. These coefficients carry crucial information regarding short-distance effects and exhibit sensitivity to BSM physics. The very low q^2 region, given the association of this decay with both left- and right-handed electromagnetic operators O_7 and O_7' , is fundamental for the determination of the C_7 and C_7' Wilson coefficients, respectively.

The $B_s^0 \rightarrow \phi e^+e^-$ differential decay rate can be written as a function of q^2 and three angular variables referred to as $\cos\theta_L$, $\cos\theta_K$ and φ . The angle θ_L (θ_K) is defined between the direction of the e^- (K^-) and the direction opposite that of the B_s^0 flight direction in the e^+e^- (K^+K^-) rest frame, while the angle φ is defined between the plane containing the two leptons and that containing the two final-state kaons in the B_s^0 rest frame. As the flavour of the B_s^0 meson at decay cannot be determined from the flavour-symmetric final state, the same angular definition is used for both B_s^0 and \bar{B}_s^0 decays, later referred to as “untagged”. As in Ref. [20], the angle φ is transformed such that $\tilde{\varphi} = \varphi + \pi$ if

¹Throughout this paper, K^{*0} is used to refer to the $K^{*0}(892)$ resonance and the inclusion of charge-conjugate processes is implied unless otherwise stated.

²The shorthand ϕ refers to the $\phi(1020)$ meson throughout this paper.

$\varphi < 0$. This transformation leads to a cancellation of the terms containing $\sin \varphi$ and $\cos \varphi$, consequently simplifying the angular expression without any loss of sensitivity to the remaining physical observables. Ignoring any K^+K^- S-wave contribution which should be negligible at low- q^2 values due to the photon-pole dominance, and in the limit of massless leptons, the normalised, untagged, time-integrated, CP -averaged angular differential decay rate is [21]

$$\begin{aligned} \frac{1}{d(\Gamma + \bar{\Gamma})/dq^2} \frac{d^3(\Gamma + \bar{\Gamma})}{d\cos\theta_L d\cos\theta_K d\tilde{\varphi}} &= \frac{9}{32\pi} \left\{ \frac{3}{4} (1 - F_L) \sin^2\theta_K + F_L \cos^2\theta_K \right. \\ &+ \left[\frac{1}{4} (1 - F_L) \sin^2\theta_K - F_L \cos^2\theta_K \right] \cos 2\theta_L \\ &+ \frac{1}{2} (1 - F_L) A_T^{(2) \sin^2\theta_K \sin^2\theta_L} \cos 2\tilde{\varphi} \\ &+ (1 - F_L) A_T^{\mathcal{R}eCP \sin^2\theta_K} \cos\theta_L \\ &\left. + \frac{1}{2} (1 - F_L) A_T^{\mathcal{I}mCP \sin^2\theta_K \sin^2\theta_L} \sin 2\tilde{\varphi} \right\}. \end{aligned} \quad (1)$$

The four angular observables F_L , $A_T^{(2)}$, $A_T^{\mathcal{I}mCP}$ and $A_T^{\mathcal{R}eCP}$ are combinations of the amplitudes $A_{0,\perp,\parallel}^{L,R}$ where the indices 0, \perp , \parallel refer to the different polarisation states of the ϕ meson in the decay, and L and R to the left- and right-hand chirality of the dielectron system. The observable F_L is the longitudinal polarisation fraction of the ϕ meson, while $A_T^{\mathcal{R}eCP}$ is related to the lepton forward-backward asymmetry. The parameters $A_T^{(2)}$ and $A_T^{\mathcal{I}mCP}$ are pivotal for this analysis as they are related to the photon polarisation and thus to the Wilson coefficients $C_7^{(\prime)}$ in the very low q^2 region. Indeed, following Ref. [21] and in the absence of decay-time acceptance, in the $q^2 \rightarrow 0$ limit, these observables can be expressed as

$$\lim_{q^2 \rightarrow 0} A_T^{(2)}(q^2) = \frac{2 \left[\mathcal{R}e[C_7] \mathcal{R}e[C_7'] + \mathcal{I}m[C_7] \mathcal{I}m[C_7'] + \frac{y}{2} [(\mathcal{R}e[C_7])^2 - (\mathcal{I}m[C_7])^2] \right]}{(\mathcal{R}e[C_7])^2 + (\mathcal{I}m[C_7])^2}, \quad (2)$$

$$\lim_{q^2 \rightarrow 0} A_T^{\mathcal{I}mCP}(q^2) = \frac{2 \left[\mathcal{R}e[C_7] \mathcal{I}m[C_7'] - \mathcal{I}m[C_7] \mathcal{R}e[C_7'] - y \mathcal{R}e[C_7] \mathcal{I}m[C_7] \right]}{(\mathcal{R}e[C_7])^2 + (\mathcal{I}m[C_7])^2}, \quad (3)$$

with $y = \frac{\Delta\Gamma_s}{2\Gamma_s}$, where $\Delta\Gamma_s$ is the difference in decay widths between the heavy and light B_s^0 mass eigenstates and Γ_s the inverse of the average lifetime of the B_s^0 meson. The F_L and $A_T^{\mathcal{R}eCP}$ parameters vanish at low values of q^2 as expected from real photon interactions.

In the SM, where C_7 is purely real, the measurement of $A_T^{\mathcal{I}mCP}$ is identical to that obtained in the similar measurement using $B^0 \rightarrow K^{*0} e^+ e^-$ decays [17], while in the case of $A_T^{(2)}$ the information is slightly different due to the significant variation in decay widths between the light and the heavy mass eigenstates in the B_s^0 system. In the future, with larger data samples, the comparison of the $A_T^{(2)}$ measurements obtained from $B_s^0 \rightarrow \phi e^+ e^-$ and $B^0 \rightarrow K^{*0} e^+ e^-$ decays could provide additional constraints on C_7 .

2 The LHCb detector and dataset

The study reported here is based on proton–proton (pp) collision data collected with the LHCb detector in the years 2011, 2012 and 2015–2018, at centre-of-mass energies of 7, 8 and 13 TeV, respectively. The total data set corresponds to an integrated luminosity of 9 fb^{-1} . The LHCb detector is a single-arm forward spectrometer covering the pseudorapidity range $2 < \eta < 5$, designed for the study of particles containing b or c quarks. The detector comprises a high-precision tracking system, including a silicon-strip vertex detector surrounding the pp interaction region, a large-area silicon-strip detector located upstream of a dipole magnet with a bending power of about 4 T m , and three stations of silicon-strip detectors and straw drift tubes placed downstream of the magnet. This tracking system provides a measurement of the momentum, p , of charged particles with a relative uncertainty ranging from 0.5% at low momentum to 1.0% at $200 \text{ GeV}/c$. The minimum distance of a track to a primary pp collision vertex (PV), known as the impact parameter (IP), is measured with a resolution of $(15 + 29/p_T) \mu\text{m}$, where p_T is the component of the momentum transverse to the beam in GeV/c . Different types of charged hadrons are distinguished using information from two ring-imaging Cherenkov detectors (RICH) [22]. Photons, electrons and hadrons are identified by a calorimeter system consisting of scintillating-pad and preshower detectors, an electromagnetic calorimeter (ECAL) and a hadronic calorimeter, along with additional information from the RICH.

An online event selection [23, 24] is performed by a trigger system that consists of a hardware stage, based on information from the calorimeter and muon systems, followed by a software stage, which applies a full event reconstruction. The hardware electron trigger requires the presence of an ECAL cluster with minimum transverse energy between 2.5 and 3.0 GeV, depending on the data-taking period. Signal $B_s^0 \rightarrow \phi e^+ e^-$ candidates are retained if at least one of the electrons fulfills the hardware electron trigger criteria or if the trigger requirements are satisfied by objects in the rest of the event that are independent of the signal B_s^0 candidate decay products. Events meeting the hardware trigger requirements are processed by the software trigger, where a two-, three- or four-track vertex with a significant displacement from any PV is required. At least one charged particle must have a significant transverse momentum and be inconsistent with originating from any PV. A multivariate algorithm is used to identify displaced vertices consistent with the decay of a b hadron [25].

Simulated samples are used to assess the effect of reconstruction and selection on the angular distributions of the signal candidates, as well as to estimate expected signal yields and contamination from specific background processes. The pp collisions are simulated using PYTHIA [26] with a specific LHCb configuration [27]. Decays of unstable particles are described by EvtGen [28], incorporating final-state radiation generated using PHOTOS [29]. The interaction of the generated particles with the detector, along with its response, is implemented using the GEANT4 toolkit [30, 31]. Residual mismodelling of the particle identification performance, the p_T spectrum of the B_s^0 mesons, the track multiplicity, and the efficiency of the hardware trigger are corrected using high-yield control samples from data, following the approach developed by the LHCb collaboration for tests of lepton universality [32].

3 Selection of signal candidates

3.1 Reconstruction

The ϕ candidates are assembled by combining charged tracks identified as K^+ and K^- mesons, ensuring the invariant mass of the K^+K^- system lies within ± 12 MeV/ c^2 of the known ϕ mass [33]. The reconstruction of $B_s^0 \rightarrow \phi e^+e^-$ candidates involves pairing the ϕ candidate with a pair of oppositely charged tracks identified as electrons. Due to bremsstrahlung photon emission, electrons lose a substantial amount of energy when interacting with detector material. A dedicated procedure, which searches for neutral transverse energy deposits larger than 75 MeV in the ECAL that are compatible with being emitted by an electron upstream of the magnet, is applied to correct for this effect. A comparison of this bremsstrahlung recovery procedure between data and simulated samples in dedicated control channels shows good agreement, thus validating correction method. However, the limitations of this recovery technique degrade the resolution of the reconstructed invariant masses of both the dielectron pair and the B_s^0 candidate. The $K^+K^-e^+e^-$ reconstructed invariant mass is therefore restricted to $4600 < m(K^+K^-e^+e^-) < 6300$ MeV/ c^2 .

The selection of the q^2 region aims to optimise the sensitivity to the photon polarisation in the $b \rightarrow s\gamma$ transition present in the $B_s^0 \rightarrow \phi e^+e^-$ decay (*i.e.* $C_7^{(\prime)}$). The reconstruction of the invariant mass-squared of the dielectron pair is performed through a kinematic fit [34], which constrains the $K^+K^-e^+e^-$ invariant mass to the known B_s^0 mass [33]. This technique, identical to the one developed in Ref. [17], improves the q^2 resolution. Subsequently, the reconstructed q^2 is required not to exceed 0.25 GeV $^2/c^4$ to minimise sensitivity to vector and axial-vector currents ($C_9^{(\prime)}$ and $C_{10}^{(\prime)}$), while maximising the retention of signal candidates. Low- q^2 signal candidates, which are particularly sensitive to $C_7^{(\prime)}$, have a poorer $\tilde{\varphi}$ resolution due to multiple scattering of quasi-collinear electrons in the tracking detectors. Additionally, contamination from $B_s^0 \rightarrow \phi\gamma$ decays, followed by photon conversion in the detector material, affects the lower end of the q^2 spectrum. Consequently, a minimum requirement of 0.0001 GeV $^2/c^4$ is imposed on the reconstructed q^2 . The use of the B_s^0 mass constraint in the kinematic fit to compute the q^2 reduces this background by 80% with respect to an unconstrained fit. The region of q^2 below 0.0001 GeV $^2/c^4$, which is enriched in $B_s^0 \rightarrow \phi\gamma$ decays, is used as a control sample and denoted as the “ γ -bin”.

Each track must exhibit a good quality and be inconsistent with originating from a PV. The kaons must have a transverse momentum larger than 400 MeV/ c and be identified as such using information from the RICH detectors. Electrons with p_T exceeding 500 MeV/ c and demonstrating a good-quality vertex are utilised to construct dielectron candidates. In events with multiple PVs, the one giving rise to the smallest value of χ_{IP}^2 is associated to the $B_s^0 \rightarrow \phi e^+e^-$ candidate.

To mitigate background pollution stemming from random track combinations (combinatorial background), a boosted decision tree (BDT) classifier, trained with the XGBoost algorithm [35], is employed. The upper mass sideband of the data samples, defined by $m(K^+K^-e^+e^-) > 5700$ MeV/ c^2 , serves as a proxy for the modelling of the combinatorial background, where statistical enrichment is achieved by relaxing the requirement on the invariant mass of the K^+K^- system (to be between 990 and 1100 MeV/ c^2). As a signal proxy, simulation samples of $B_s^0 \rightarrow \phi e^+e^-$ candidates are used. A k -fold cross-validation

approach with $k = 10$ is used [36], in which each of the ten classifiers is trained leaving out a different 10% of the data sample. The classifier uses eight kinematic and decay-topology variables, notably including information on the impact parameter of final-state particles, as well as the transverse momentum of the B_s^0 candidate and its flight distance. Other variables include the angle between the B_s^0 momentum and its flight distance vector, the fit quality of the B_s^0 vertex, and its displacement from the associated PV. The classifier reduces the background level by half while retaining 99% of the signal.

3.2 Exclusive backgrounds

Various sources of specific backgrounds are studied using dedicated simulation samples. Identified background sources expected to contribute at a level greater than 1% of the expected signal are modelled and included in the angular fit described in Sec. 4.

A significant background pollution arises from semileptonic $B_s^0 \rightarrow D_s^- (\rightarrow \phi e^- \bar{\nu}_e) e^+ \nu_e$ decays which share a common final state with the signal given that the neutrinos are not reconstructed. This background populates the region below the B_s^0 invariant mass and has a combined branching fraction about four orders of magnitude larger than that of the signal [33]. Even though the vast majority of this background populates higher q^2 regions, when both neutrinos possess low energies the effectiveness of the signal selection in rejecting this background diminishes. For this background, the positron from the B_s^0 decay tends to exhibit higher energy than the electron from the D_s^- decay. Consequently, the reconstructed $\cos \theta_L$ distribution tends to favor larger values, as $\cos \theta_L$ is highly correlated with the e^+e^- energy asymmetry. As a result, a symmetric requirement $|\cos \theta_L| < 0.9$ is imposed to further suppress this background. While this leads to a 1% loss of signal, it removes 40% of this semileptonic background, sufficient that it can be subsequently neglected in the fit. Additionally, the contribution from the $B_s^0 \rightarrow D_s^{*-} (\rightarrow \phi e^- \bar{\nu}_e) e^+ \nu_e$ mode is also studied. It is found to be smaller than the D_s^- one by a factor 0.63, and therefore negligible.

The radiative $B_s^0 \rightarrow \phi \gamma$ branching fraction is approximately two orders of magnitude larger than that of the signal [33], featuring a very similar distribution in the reconstructed $K^+K^-e^+e^-$ invariant mass. In the very low q^2 region, the contamination from $B_s^0 \rightarrow \phi \gamma$ decays is measured to be at the level of 15%, but is reduced to about 3% by applying a conversion veto rejecting $\gamma \rightarrow e^+e^-$ processes compatible with originating from detector material.

Candidates from $B_s^0 \rightarrow \phi \eta$ and $B_s^0 \rightarrow \phi \pi^0$ decays, where the η or π^0 meson decays through the $e^+e^- \gamma$ Dalitz process [37], can pass the selection if the photon has low energy, or if it is recovered as a bremsstrahlung photon. In the latter case, the reconstructed $K^+K^-e^+e^-$ invariant-mass peaks at the B_s^0 invariant mass. The branching fraction of the η and π^0 Dalitz decays are assumed to be similar to the corresponding B^0 decays [33] and their contamination are estimated to be at the level of 4.7% and 1.8%, respectively.

Background contributions from misidentified $B_s^0 \rightarrow \phi (\rightarrow K^+K^-) \phi (\rightarrow K^+K^-)$, $B^0 \rightarrow K^{*0} (\rightarrow K^+\pi^-) e^+e^-$ and $\Lambda_b^0 \rightarrow p K^- e^+e^-$ decays are studied but are found to be negligible, due to a low electron misidentification rate ($\sim 2\%$) and the narrowness of the ϕ resonance.

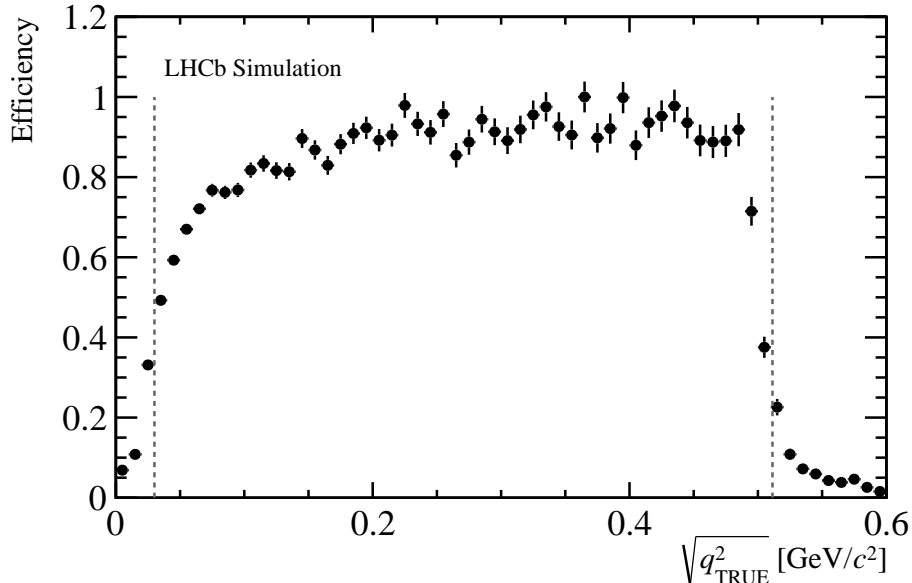


Figure 1: Relative efficiency as a function of the true dielectron invariant mass ($\sqrt{q_{\text{TRUE}}^2}$). The points represent the efficiency obtained from simulation, while the vertical lines represent the effective boundaries ($\sqrt{q_{\text{TRUE}}^2}$ between $30 \text{ MeV}/c^2$ and $511 \text{ MeV}/c^2$). The use of $\sqrt{q_{\text{TRUE}}^2}$ instead of q_{TRUE}^2 allows for better visualisation of the boundary effects.

3.3 Effective q^2 range of the $B_s^0 \rightarrow \phi e^+ e^-$ signal events

The dependence of the signal efficiency as a function of the true dielectron invariant mass, as determined through simulation, is shown in Fig. 1. This efficiency is slowly varying in most of the signal region. Close to the boundaries, the efficiency drops rapidly due to the selected range of reconstructed q^2 and the effect of the dielectron mass resolution. Therefore, following the method described in Ref. [20], effective q^2 boundaries are defined to be located between $0.0009 \text{ GeV}^2/c^4$ and $0.2615 \text{ GeV}^2/c^4$ to allow for theoretical predictions of the angular observables without any input from simulation.

4 Angular analysis

The angular observables F_L , $A_{\text{T}}^{(2)}$, A_{T}^{ImCP} and A_{T}^{ReCP} , defined in Eq. (1), are determined through a four-dimensional unbinned maximum-likelihood fit to the $m(K^+K^-e^+e^-)$, $\cos\theta_L$, $\cos\theta_K$, and $\tilde{\varphi}$ distributions. After the selection, the $K^+K^-e^+e^-$ invariant mass does not exhibit correlation with the angular distributions as indicated by simulation. The $m(K^+K^-e^+e^-)$ distribution is thus incorporated into the fit to enhance the discrimination power between signal and background. Both signal and $B_s^0 \rightarrow \phi\gamma$ invariant-mass components are represented by a double-sided Crystal Ball function [38] that consists of a Gaussian core with asymmetric power-law tails. The tail parameters are fixed to the values obtained from simulation. The widths and mean values are corrected for differences between data and simulation obtained from the γ -bin fit results.

The angular distributions of the signal candidates are parameterised by the product of

Eq. (1) and a function describing the angular acceptance of the candidate reconstruction and selection process. A dedicated simulated sample generated with flat angular distributions is used to model the angular acceptance, assuming factorization of the three angles: $\epsilon(\cos\theta_L, \cos\theta_K, \tilde{\varphi}) = \epsilon(\cos\theta_L) \times \epsilon(\cos\theta_K) \times \epsilon(\tilde{\varphi})$. The acceptance is parameterised using Legendre polynomials of order eight for $\cos\theta_L$ and order four for $\cos\theta_K$. Given the flavour-symmetric final state, only even orders are considered. For the $\tilde{\varphi}$ angle, nonuniform acceptance terms proportional to $\cos(2\tilde{\varphi})$ and $\sin(2\tilde{\varphi})$ are allowed. However, no significant deviation from a uniform distribution is observed.

The combinatorial background in $m(K^+K^-e^+e^-)$ is described by an exponential function whose slope is a free parameter in the fit. The modelling of the angular distribution relies on constraints obtained using a data sample reconstructed as $B_s^0 \rightarrow \phi e^\pm \mu^\mp$. Indeed, as this decay is forbidden in the SM due to lepton-flavour conservation, the sample mostly comprises semileptonic and combinatorial background candidates. The q^2 and selection requirements are slightly changed to account for the muon in the final state. The $\cos\theta_L$ and $\cos\theta_K$ are modelled separately by Legendre polynomials and the $\tilde{\varphi}$ distribution is assumed to be uniform. It is verified that the $B_s^0 \rightarrow \phi e^\pm \mu^\mp$ sample is a good proxy for the combinatorial background by comparing the invariant mass and angular distributions to those of $B_s^0 \rightarrow \phi e^+e^-$ decays in the lower ($< 5100 \text{ MeV}/c^2$) and upper ($> 5500 \text{ MeV}/c^2$) mass sideband regions.

For the $B_s^0 \rightarrow \phi\gamma$ background, the electrons originate from the interaction of a real photon with detector material. Hence, the $\cos\theta_L$ and $\tilde{\varphi}$ dependent parts of Eq. (1) can be integrated out to model only the $\cos\theta_K$ dependent part. This shape is dependent solely on the parameter F_L . The value of F_L for the $B_s^0 \rightarrow \phi\gamma$ decay is obtained from the fit to the γ -bin. When included as a background in the fit to the signal sample, its angular shape in $\cos\theta_L$ and $\tilde{\varphi}$ is derived from a simulated sample and is assumed to factorise between the angles.

The shapes of the $B_s^0 \rightarrow \phi\eta$ and $B_s^0 \rightarrow \phi\pi^0$ background contributions are modelled using simulated samples through nonparametric probability density functions [39] for the invariant mass and via Chebychev polynomials for the angles.

The fitting procedure is validated using a large sample of simulated $B_s^0 \rightarrow \phi e^+e^-$ signal decays with a size about 500 times that of the signal yield on data, where the measured values of F_L , $A_T^{(2)}$, $A_T^{\mathcal{I}mCP}$, and $A_T^{\mathcal{R}eCP}$ are in agreement with the generated values demonstrating, in particular, the validity of the modelling of the angular acceptance. Subsequently, the $B_s^0 \rightarrow \phi e^+e^-$ fit model is validated against data through a two-dimensional fit to the $m(K^+K^-e^+e^-)$ and $\cos\theta_K$ distributions of the $B_s^0 \rightarrow \phi\gamma$ control sample, corresponding to a total of around 580 signal candidates. The results from this fit, including their projections, are illustrated in Fig. 2. The obtained value of $F_L = -0.01 \pm 0.02$, where the uncertainty is statistical only, agrees well with a purely transverse polarisation of the ϕ meson, indicative of a real photon interaction.

An additional validation is conducted through pseudoexperiments that include both signal and background components with yields obtained from the data fit, where the angular observables F_L , $A_T^{(2)}$, $A_T^{\mathcal{I}mCP}$, and $A_T^{\mathcal{R}eCP}$ are generated according to their SM predictions. The results show good compatibility with the input parameters, with the exception of a minor bias in F_L , quantified as 0.14% of its statistical uncertainty. This bias is due to the vicinity of the physical boundary at zero, therefore an upper limit on F_L is computed using a Feldman–Cousins approach [40].

Table 1: Summary of the systematic uncertainties. For comparison, the statistical uncertainties are shown in the last row of the table. The dash indicates that the parameter is not affected by the corresponding systematic.

Source of systematic	$A_T^{(2)}$	A_T^{ImCP}	A_T^{ReCP}	F_L
$\Delta\Gamma_s/\Gamma_s$	0.008	<0.001	<0.001	<0.001
Corrections to simulation	0.002	<0.001	<0.001	0.010
Acceptance function modelling	<0.001	<0.001	0.001	0.002
Simulation sample size for acceptance	0.006	0.008	0.005	0.002
Background contamination	0.009	0.014	0.004	0.006
Angles resolution	-0.005	<0.001	—	—
Total systematic uncertainty	0.014	0.016	0.006	0.012
Statistical uncertainty	0.235	0.247	0.155	0.056

5 Systematic uncertainties

A summary of the systematic uncertainties is shown in Table 1. They are estimated using pseudoexperiments generated according to the baseline result. The pseudoexperiments are fitted with both the default and alternative models, and the resulting difference in angular observables is assigned as the systematic uncertainty.

All simulated samples used in the analysis are generated with the $\Delta\Gamma_s$ parameter set to zero. A systematic uncertainty is computed by altering the angular, q^2 , and B_s^0 lifetime distributions of simulated samples to reflect the current world average value $\frac{\Delta\Gamma_s}{\Gamma_s} = 0.126$ [33], primarily affecting the value of $A_T^{(2)}$.

The systematic uncertainties associated with the corrections applied to simulated candidates used to model the angular acceptance are evaluated by fitting uncorrected simulated candidates. An alternative model using Legendre polynomials with odd coefficients is used to estimate the systematic uncertainties associated with the shape of the acceptance function. To compute the uncertainty linked to the size of the sample used to extract the acceptance shape, the acceptance parameters in pseudoexperiments are randomly generated within one standard deviation. Peaking background contributions are evaluated by varying the contamination of each background component within its

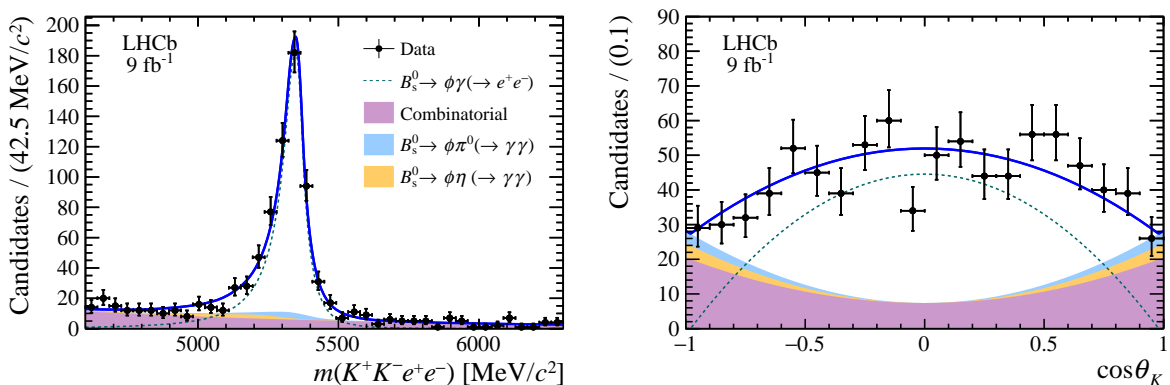


Figure 2: Distributions of the (left) $K^+K^-e^+e^-$ invariant mass and (right) $\cos\theta_K$ of the $B_s^0 \rightarrow \phi\gamma$ control sample, with the fit projection also shown.

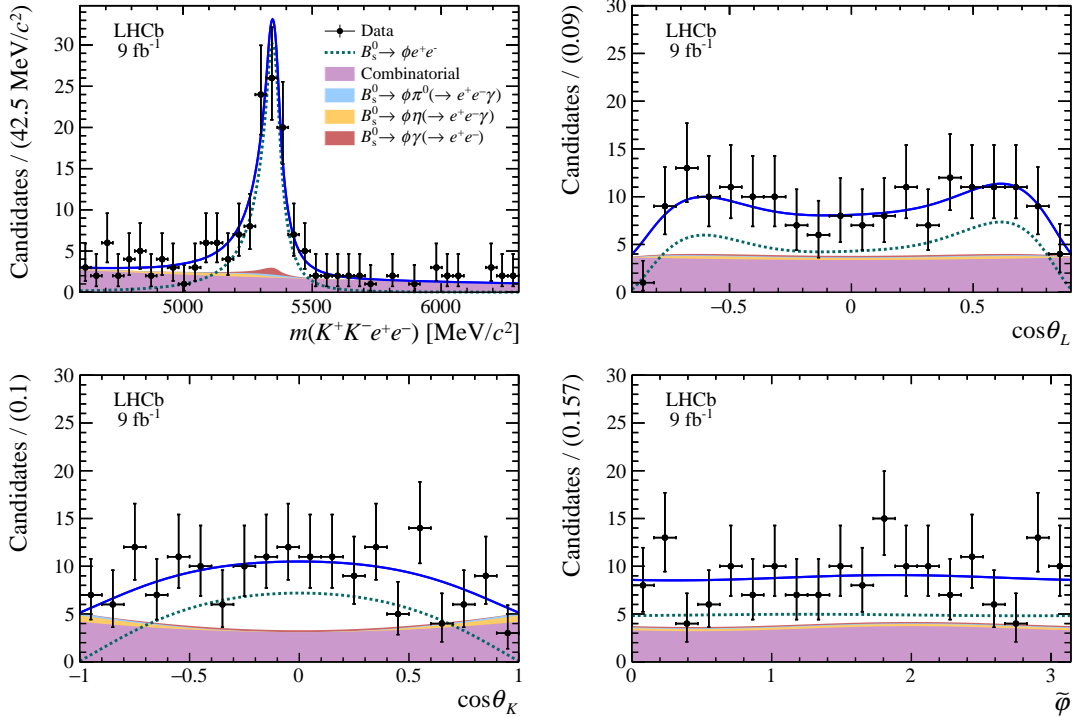


Figure 3: Distributions of the (top left) $K^+K^-e^+e^-$ invariant mass, (top right) $\cos\theta_L$, (bottom left) $\cos\theta_K$ and (bottom right) $\tilde{\varphi}$ of $B_s^0 \rightarrow \phi e^+ e^-$ candidates in the very low q^2 range with fit projections also shown.

uncertainty.

Furthermore, the non-negligible size of the $\tilde{\varphi}$ resolution results in an underestimation of the magnitude of $A_T^{(2)}$ proportional to its value. The size of the effect is estimated using signal-only pseudoexperiments generated with a q^2 -dependent smearing on $\tilde{\varphi}$ and fitted with the default fitting function which ignores this resolution effect.

It is checked that other sources of systematic uncertainties, such as the signal invariant-mass model and combinatorial angular modelling, yield negligible contributions to the overall systematic uncertainty. This is expected since the related parameters are only loosely constrained in the fit.

The total systematic uncertainties are obtained by summing all contributions in quadrature, and are, in all cases, to be smaller than the statistical uncertainties on the observables.

6 Results

The projections of the final fit on $m(K^+K^-e^+e^-)$ and the three angles are displayed in Fig. 3. The total signal yield observed within the effective q^2 range, from 0.0009 to 0.2615 GeV^2/c^4 , is about 100 events. Together with the results from Ref. [41], this constitutes the first observation of the $B_s^0 \rightarrow \phi e^+ e^-$ decay mode.

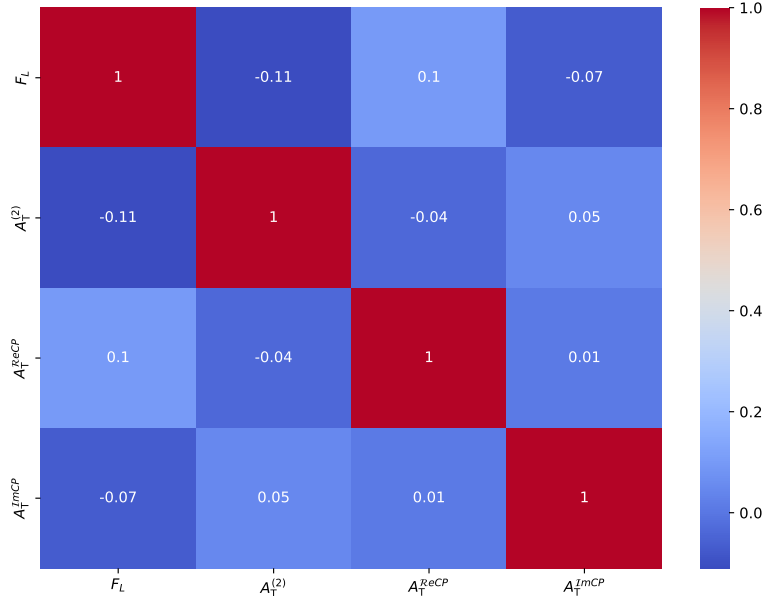


Figure 4: The statistical correlation matrix for the four angular parameters in the final fit.

The obtained values for the four angular observables are

$$\begin{aligned}
 A_T^{(2)} &= -0.045 \pm 0.235 \pm 0.014, \\
 A_T^{ImCP} &= 0.002 \pm 0.247 \pm 0.016, \\
 A_T^{ReCP} &= 0.116 \pm 0.155 \pm 0.006, \\
 F_L &= (0.4 \pm 5.6 \pm 1.2)\%,
 \end{aligned}$$

where the first uncertainty is statistical and the second systematic. Fig. 4 presents the heatmap of the correlation matrix for the four angular parameters from the final fit. Given the full dominance of the statistical uncertainties, it is not significantly altered by the systematical ones. As the F_L parameter is close to the physical boundary, the Feldman–Cousins method is applied to determine an upper limit, $F_L < 11.5\%$ (13.7%) at the 90% (95%) confidence level (CL). A shift of -0.025 has been applied to the $A_T^{(2)}$ parameter to correct for the remaining bias observed while fitting the simulation corrected for the $\Delta\Gamma_s$ being nonzero. Studies with simulation show that this bias arises from the nonuniform efficiency in the B_s^0 decay time.

7 Summary

An angular analysis of the $B_s^0 \rightarrow \phi e^+ e^-$ decay is performed for the first time, using pp collision data collected by the LHCb experiment between 2011 and 2018, corresponding to an integrated luminosity of 9 fb^{-1} . Angular observables are measured in an effective q^2 region between 0.0009 and $0.2615 \text{ GeV}^2/c^4$. The results are consistent with the SM predictions [21, 42–44]. Using the `flavio` software package [43], they can be used to measure both the real and imaginary parts of the $B_s^0 \rightarrow \phi\gamma$ photon polarisation with a precision of 12%. The $C_7^{(\prime)}$ regularisation-scheme-independent effective coefficients are calculated at

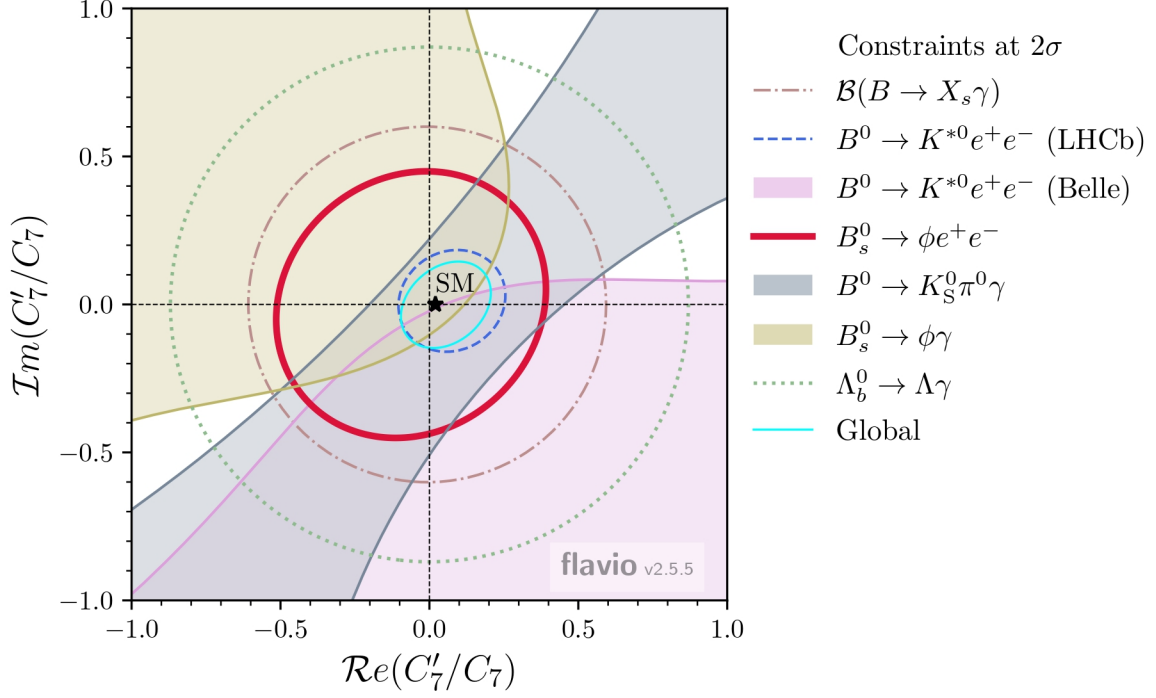


Figure 5: Current constraints at the 2σ level (containing 95.4% of the distribution) on the real and imaginary part of the ratio of the right- to left-handed Wilson coefficients C'_7 and C_7 . The constraints from various measurements are shown in light colours and are, for most of them, the combination of several results. The constraints from angular analyses of $B^0 \rightarrow K^{*0} e^+ e^-$ decays from the LHCb and the Belle experiments are performed in different q^2 regions and are shown separately. The constraints from the measurement presented in this paper are shown in red and the result of the global fit in cyan. The SM prediction is represented by the black star.

the scale $\mu = 4.8 \text{ GeV}$ [45] and the value of the left-handed C_7 coefficient is fixed to its SM value, -0.2915 . The overall constraints, shown in Fig. 5, are compared to those from previous measurements from the BaBar, Belle, Belle II and LHCb collaborations [7–17].

Acknowledgements

We express our gratitude to our colleagues in the CERN accelerator departments for the excellent performance of the LHC. We thank the technical and administrative staff at the LHCb institutes. We acknowledge support from CERN and from the national agencies: CAPES, CNPq, FAPERJ and FINEP (Brazil); MOST and NSFC (China); CNRS/IN2P3 (France); BMBF, DFG and MPG (Germany); INFN (Italy); NWO (Netherlands); MNiSW and NCN (Poland); MCID/IFA (Romania); MICIU and AEI (Spain); SNSF and SER (Switzerland); NASU (Ukraine); STFC (United Kingdom); DOE NP and NSF (USA). We acknowledge the computing resources that are provided by CERN, IN2P3 (France), KIT and DESY (Germany), INFN (Italy), SURF (Netherlands), PIC (Spain), GridPP (United Kingdom), CSCS (Switzerland), IFIN-HH (Romania), CBPF (Brazil), and Polish WLCG (Poland). We are indebted to the communities behind the multiple open-source software packages on which we depend. Individual groups or members have received support from ARC and ARDC (Australia); Key Research Program of Frontier Sciences of CAS, CAS PIFI, CAS CCEPP, Fundamental Research Funds for the Central Universities, and Sci. & Tech. Program of Guangzhou (China); Minciencias (Colombia); EPLANET, Marie Skłodowska-Curie Actions, ERC and NextGenerationEU (European Union); A*MIDEX, ANR, IPhU and Labex P2IO, and Région Auvergne-Rhône-Alpes (France); AvH Foundation (Germany); ICSC (Italy); Severo Ochoa and María de Maeztu Units of Excellence, GVA, XuntaGal, GENCAT, InTalent-Inditex and Prog. Atracción Talento CM (Spain); SRC (Sweden); the Leverhulme Trust, the Royal Society and UKRI (United Kingdom).

References

- [1] D. Atwood, M. Gronau, and A. Soni, *Mixing-induced CP asymmetries in radiative B decays in and beyond the standard model*, *Phys. Rev. Lett.* **79** (1997) 185, [arXiv:hep-ph/9704272](#).
- [2] L. L. Everett *et al.*, *Alternative approach to $b \rightarrow s\gamma$ in the uMSSM*, *JHEP* **01** (2002) 022, [arXiv:hep-ph/0112126](#).
- [3] B. Grinstein, Y. Grossman, Z. Ligeti, and D. Pirjol, *Photon polarization in $B \rightarrow X\gamma$ in the standard model*, *Phys. Rev.* **D71** (2005) 011504, [arXiv:hep-ph/0412019](#).
- [4] J. Foster, K.-i. Okumura, and L. Roszkowski, *New constraints on SUSY flavour mixing in light of recent measurements at the Tevatron*, *Phys. Lett.* **B641** (2006) 452, [arXiv:hep-ph/0604121](#).
- [5] E. Lunghi and J. Matias, *Huge right-handed current effects in $B \rightarrow K^{*0}(K\pi^0)\ell^+\ell^-$ in supersymmetry*, *JHEP* **04** (2007) 058, [arXiv:hep-ph/0612166](#).
- [6] D. Bečirević, E. Kou, A. Le Yaouanc, and A. Tayduganov, *Future prospects for the determination of the Wilson coefficient $C'_{7\gamma}$* , *JHEP* **08** (2012) 090, [arXiv:1206.1502](#).
- [7] BaBar collaboration, B. Aubert *et al.*, *Measurement of the $B \rightarrow X_s\gamma$ branching fraction and photon energy spectrum using the recoil method*, *Phys. Rev.* **D77** (2008) 051103, [arXiv:0711.4889](#).
- [8] BaBar collaboration, J. P. Lees *et al.*, *Precision measurement of the $B \rightarrow X_s\gamma$ photon energy spectrum, branching fraction and direct CP asymmetry $A_{CP}(B \rightarrow X_{s+d}\gamma)$* , *Phys. Rev. Lett.* **109** (2012) 191801, [arXiv:1207.2690](#).
- [9] BaBar collaboration, J. P. Lees *et al.*, *Exclusive measurements of $b \rightarrow s\gamma$ transition rate and photon energy spectrum*, *Phys. Rev.* **D86** (2012) 052012, [arXiv:1207.2520](#).
- [10] Belle collaboration, T. Saito *et al.*, *Measurement of the $\bar{B} \rightarrow X_s\gamma$ branching fraction with a sum of exclusive decays*, *Phys. Rev.* **D91** (2015) 052004, [arXiv:1411.7198](#).
- [11] Belle collaboration, *Measurement of the inclusive $B \rightarrow X_{s+d}\gamma$ branching fraction, photon energy spectrum and HQE parameters*, [arXiv:1608.02344](#).
- [12] Belle collaboration, Y. Ushiroda *et al.*, *Time-dependent CP asymmetries in $B \rightarrow K_S^0\pi^0\gamma$ transitions*, *Phys. Rev.* **D74** (2006) 111104, [arXiv:hep-ex/0608017](#).
- [13] Belle Collaboration, D. Ferlewicz *et al.*, *Angular analysis of $B \rightarrow K^*e^+e^-$ in the low- q^2 region with new electron identification at Belle*, *Phys. Rev. D* **110** (2024) 072005, [arXiv:2404.00201](#).
- [14] Belle II collaboration, I. Adachi *et al.*, *Measurement of CP asymmetries in $B^0 \rightarrow K_S^0\pi^0\gamma$ decays at Belle II*, [arXiv:2407.09139](#).
- [15] LHCb collaboration, R. Aaij *et al.*, *Measurement of CP-violating and mixing-induced observables in $B_s^0 \rightarrow \phi\gamma$ decays*, *Phys. Rev. Lett.* **123** (2019) 081802, [arXiv:1905.06284](#).

- [16] LHCb collaboration, R. Aaij *et al.*, *Measurement of the photon polarization in $\Lambda_b^0 \rightarrow \Lambda \gamma$ decays*, *Phys. Rev.* **D105** (2022) 051104, [arXiv:2111.10194](#).
- [17] LHCb collaboration, R. Aaij *et al.*, *Strong constraints on the $b \rightarrow s \gamma$ photon polarisation from $B^0 \rightarrow K^{*0} e^+ e^-$ decays*, *JHEP* **12** (2020) 081, [arXiv:2010.06011](#).
- [18] A. Bharucha, D. M. Straub, and R. Zwicky, *$B \rightarrow V \ell^+ \ell^-$ in the Standard Model from light-cone sum rules*, *JHEP* **2016** (2016) 098, [arXiv:1503.05534](#).
- [19] P. Ball, G. W. Jones, and R. Zwicky, *$B \rightarrow V \gamma$ beyond QCD factorization*, *Phys. Rev.* **D75** (2007) , [arXiv:hep-ph/0612081](#).
- [20] LHCb collaboration, R. Aaij *et al.*, *Angular analysis of the $B^0 \rightarrow K^{*0} e^+ e^-$ decay in the low- q^2 region*, *JHEP* **04** (2015) 064, [arXiv:1501.03038](#).
- [21] S. Descotes-Genon, I. Plakias, and O. Sumensari, *On the impact of meson mixing on $B_s \rightarrow \phi e e$ angular observables at low q^2* , *JHEP* **02** (2023) 096, [arXiv:2210.11995](#).
- [22] M. Adinolfi *et al.*, *Performance of the LHCb RICH detector at the LHC*, *Eur. Phys. J.* **C73** (2013) 2431, [arXiv:1211.6759](#).
- [23] R. Aaij *et al.*, *The LHCb trigger and its performance in 2011*, *JINST* **8** (2013) P04022, [arXiv:1211.3055](#).
- [24] R. Aaij *et al.*, *Design and performance of the LHCb trigger and full real-time reconstruction in Run 2 of the LHC*, *JINST* **14** (2019) P04013, [arXiv:1812.10790](#).
- [25] V. V. Gligorov and M. Williams, *Efficient, reliable and fast high-level triggering using a bonsai boosted decision tree*, *JINST* **8** (2013) P02013, [arXiv:1210.6861](#).
- [26] T. Sjöstrand, S. Mrenna, and P. Skands, *A brief introduction to PYTHIA 8.1*, *Comput. Phys. Commun.* **178** (2008) 852, [arXiv:0710.3820](#).
- [27] I. Belyaev *et al.*, *Handling of the generation of primary events in Gauss, the LHCb simulation framework*, *J. Phys. Conf. Ser.* **331** (2011) 032047.
- [28] D. J. Lange, *The EvtGen particle decay simulation package*, *Nucl. Instrum. Meth.* **A462** (2001) 152.
- [29] N. Davidson, T. Przedzinski, and Z. Was, *PHOTOS interface in C++: Technical and physics documentation*, *Comp. Phys. Comm.* **199** (2016) 86, [arXiv:1011.0937](#).
- [30] Geant4 collaboration, J. Allison *et al.*, *Geant4 developments and applications*, *IEEE Trans. Nucl. Sci.* **53** (2006) 270.
- [31] M. Clemencic *et al.*, *The LHCb simulation application, Gauss: Design, evolution and experience*, *J. Phys. Conf. Ser.* **331** (2011) 032023.
- [32] LHCb collaboration, R. Aaij *et al.*, *Measurement of lepton universality parameters in $B^+ \rightarrow K^+ \ell^+ \ell^-$ and $B^0 \rightarrow K^{*0} \ell^+ \ell^-$ decays*, *Phys. Rev.* **D108** (2023) 032002, [arXiv:2212.09153](#).

- [33] Particle Data Group, S. Navas *et al.*, *Review of particle physics*, *Phys. Rev.* **D110** (2024) 030001.
- [34] W. D. Hulsbergen, *Decay chain fitting with a Kalman filter*, *Nucl. Instrum. Meth.* **A552** (2005) 566, [arXiv:physics/0503191](#).
- [35] T. Chen and C. Guestrin, *XGBoost: a scalable tree boosting system*, in *Proceedings of the 22nd ACM SIGKDD International Conference on Knowledge Discovery and Data Mining*, KDD '16, (New York, NY, USA), 785–794, Association for Computing Machinery, 2016, [arXiv:1603.02754](#).
- [36] A. Blum, A. Kalai, and J. Langford, *Beating the hold-out: bounds for k-fold and progressive cross-validation*, in *Proceedings of the Twelfth Annual Conference on Computational Learning Theory*, COLT '99, (New York, NY, USA), 203–208, Association for Computing Machinery, 1999.
- [37] R. H. Dalitz, *On an alternative decay process for the neutral π -meson*, *Proceedings of the Physical Society. Section A* **64** (1951) 667.
- [38] T. Skwarnicki, *A study of the radiative cascade transitions between the Upsilon-prime and Upsilon resonances*, PhD thesis, Institute of Nuclear Physics, Krakow, 1986, [DESY-F31-86-02](#).
- [39] K. Cranmer, *Kernel estimation in high-energy physics*, *Computer Physics Communications* **136** (2001) 198–207, [arXiv:hep-ex/0011057](#).
- [40] G. J. Feldman and R. D. Cousins, *Unified approach to the classical statistical analysis of small signals*, *Phys. Rev.* **D57** (1998) 3873, [arXiv:physics/9711021](#).
- [41] LHCb collaboration, R. Aaij *et al.*, *Test of lepton flavour universality with $B_s^0 \rightarrow \phi \ell^+ \ell^-$ decays*, [arXiv:2410.13748](#), Submitted to *Phys. Rev. Lett.*
- [42] D. Bečirević and E. Schneider, *On transverse asymmetries in $B \rightarrow K^* \ell^+ \ell^-$* , *Nucl. Phys.* **B854** (2012) 321–339, [arXiv:1106.3283](#).
- [43] D. M. Straub, *flavio: a Python package for flavour and precision phenomenology in the Standard Model and beyond*, [arXiv:1810.08132](#).
- [44] S. Jäger and J. Martin Camalich, *Reassessing the discovery potential of the $B \rightarrow K^* \ell^+ \ell^-$ decays in the large-recoil region: SM challenges and BSM opportunities*, *Phys. Rev.* **D93** (2016) 014028, [arXiv:1412.3183](#).
- [45] A. Paul and D. M. Straub, *Constraints on new physics from radiative B decays*, *JHEP* **2017** (2017) , [arXiv:1608.02556](#).

C. Trippel⁴⁵ , G. Tuci²² , N. Tuning³⁸ , L.H. Uecker²² , A. Ukleja⁴⁰ ,
D.J. Unverzagt²² , E. Ursov⁴⁴ , A. Usachov³⁹ , A. Ustyuzhanin⁴⁴ , U. Uwer²² ,
V. Vagnoni²⁵ , V. Valcarce Cadenas⁴⁷ , G. Valenti²⁵ , N. Valls Canudas⁴⁹ ,
H. Van Hecke⁶⁸ , E. van Herwijnen⁶² , C.B. Van Hulse^{47,x} , R. Van Laak⁵⁰ ,
M. van Veghel³⁸ , G. Vazquez⁵¹ , R. Vazquez Gomez⁴⁶ , P. Vazquez Regueiro⁴⁷ ,
C. Vázquez Sierra⁴⁷ , S. Vecchi²⁶ , J.J. Velthuis⁵⁵ , M. Veltri^{27,w} ,
A. Venkateswaran⁵⁰ , M. Verdoglia³² , M. Vesterinen⁵⁷ , D. Vico Benet⁶⁴ , P.
Vidrier Villalba⁴⁶ , M. Vieites Diaz⁴⁹ , X. Vilasis-Cardona⁴⁵ , E. Vilella Figueras⁶¹ ,
A. Villa²⁵ , P. Vincent¹⁶ , F.C. Volle⁵⁴ , D. vom Bruch¹³ , N. Voropaev⁴⁴ , K. Vos⁷⁹ ,
G. Vouters¹⁰ , C. Vrahas⁵⁹ , J. Wagner¹⁹ , J. Walsh³⁵ , E.J. Walton^{1,57} , G. Wan⁶ ,
C. Wang²² , G. Wang⁸ , J. Wang⁶ , J. Wang⁵ , J. Wang^{4,b} , J. Wang⁷⁴ ,
M. Wang³⁰ , N. W. Wang⁷ , R. Wang⁵⁵ , X. Wang⁸ , X. Wang⁷² , X. W. Wang⁶² ,
Y. Wang⁶ , Z. Wang¹⁴ , Z. Wang^{4,b} , Z. Wang³⁰ , J.A. Ward^{57,1} , M. Waterlaet⁴⁹ ,
N.K. Watson⁵⁴ , D. Websdale⁶² , Y. Wei⁶ , J. Wendel⁸¹ , B.D.C. Westhenry⁵⁵ ,
C. White⁵⁶ , M. Whitehead⁶⁰ , E. Whiter⁵⁴ , A.R. Wiederhold⁶³ , D. Wiedner¹⁹ ,
G. Wilkinson⁶⁴ , M.K. Wilkinson⁶⁶ , M. Williams⁶⁵ , M. J. Williams⁴⁹ ,
M.R.J. Williams⁵⁹ , R. Williams⁵⁶ , Z. Williams⁵⁵ , F.F. Wilson⁵⁸ , M. Winn¹² ,
W. Wislicki⁴² , M. Witek⁴¹ , L. Witola²² , G. Wormser¹⁴ , S.A. Wotton⁵⁶ , H. Wu⁶⁹ ,
J. Wu⁸ , X. Wu⁷⁴ , Y. Wu⁶ , Z. Wu⁷ , K. Wyllie⁴⁹ , S. Xian⁷² , Z. Xiang⁵ , Y. Xie⁸ ,
A. Xu³⁵ , J. Xu⁷ , L. Xu^{4,b} , L. Xu^{4,b} , M. Xu⁵⁷ , Z. Xu⁴⁹ , Z. Xu⁷ , Z. Xu⁵ ,
D. Yang⁴ , K. Yang⁶² , S. Yang⁷ , X. Yang⁶ , Y. Yang^{29,m} , Z. Yang⁶ , Z. Yang⁶⁷ ,
V. Yeroshenko¹⁴ , H. Yeung⁶³ , H. Yin⁸ , X. Yin⁷ , C. Y. Yu⁶ , J. Yu⁷¹ ,
X. Yuan⁵ , Y. Yuan^{5,7} , E. Zaffaroni⁵⁰ , M. Zavertyaev²¹ , M. Zdybal⁴¹ ,
F. Zenesini^{25,j} , C. Zeng^{5,7} , M. Zeng^{4,b} , C. Zhang⁶ , D. Zhang⁸ , J. Zhang⁷ ,
L. Zhang^{4,b} , S. Zhang⁷¹ , S. Zhang⁶⁴ , Y. Zhang⁶ , Y. Z. Zhang^{4,b} , Y. Zhao²² ,
A. Zharkova⁴⁴ , A. Zhelezov²² , S. Z. Zheng⁶ , X. Z. Zheng^{4,b} , Y. Zheng⁷ ,
T. Zhou⁶ , X. Zhou⁸ , Y. Zhou⁷ , V. Zhovkovska⁵⁷ , L. Z. Zhu⁷ , X. Zhu^{4,b} ,
X. Zhu⁸ , V. Zhukov¹⁷ , J. Zhuo⁴⁸ , Q. Zou^{5,7} , D. Zuliani^{33,p} , G. Zunica⁵⁰ .

¹School of Physics and Astronomy, Monash University, Melbourne, Australia

²Centro Brasileiro de Pesquisas Físicas (CBPF), Rio de Janeiro, Brazil

³Universidade Federal do Rio de Janeiro (UFRJ), Rio de Janeiro, Brazil

⁴Department of Engineering Physics, Tsinghua University, Beijing, China

⁵Institute Of High Energy Physics (IHEP), Beijing, China

⁶School of Physics State Key Laboratory of Nuclear Physics and Technology, Peking University, Beijing, China

⁷University of Chinese Academy of Sciences, Beijing, China

⁸Institute of Particle Physics, Central China Normal University, Wuhan, Hubei, China

⁹Consejo Nacional de Rectores (CONARE), San Jose, Costa Rica

¹⁰Université Savoie Mont Blanc, CNRS, IN2P3-LAPP, Annecy, France

¹¹Université Clermont Auvergne, CNRS/IN2P3, LPC, Clermont-Ferrand, France

¹²Université Paris-Saclay, Centre d'Etudes de Saclay (CEA), IRFU, Saclay, France, Gif-Sur-Yvette, France

¹³Aix Marseille Univ, CNRS/IN2P3, CPPM, Marseille, France

¹⁴Université Paris-Saclay, CNRS/IN2P3, IJCLab, Orsay, France

¹⁵Laboratoire Leprince-Ringuet, CNRS/IN2P3, Ecole Polytechnique, Institut Polytechnique de Paris, Palaiseau, France

¹⁶LPNHE, Sorbonne Université, Paris Diderot Sorbonne Paris Cité, CNRS/IN2P3, Paris, France

¹⁷I. Physikalisches Institut, RWTH Aachen University, Aachen, Germany

¹⁸Universität Bonn - Helmholtz-Institut für Strahlen und Kernphysik, Bonn, Germany

¹⁹Fakultät Physik, Technische Universität Dortmund, Dortmund, Germany

²⁰Physikalisches Institut, Albert-Ludwigs-Universität Freiburg, Freiburg, Germany

²¹Max-Planck-Institut für Kernphysik (MPIK), Heidelberg, Germany

- ²² *Physikalisches Institut, Ruprecht-Karls-Universität Heidelberg, Heidelberg, Germany*
- ²³ *School of Physics, University College Dublin, Dublin, Ireland*
- ²⁴ *INFN Sezione di Bari, Bari, Italy*
- ²⁵ *INFN Sezione di Bologna, Bologna, Italy*
- ²⁶ *INFN Sezione di Ferrara, Ferrara, Italy*
- ²⁷ *INFN Sezione di Firenze, Firenze, Italy*
- ²⁸ *INFN Laboratori Nazionali di Frascati, Frascati, Italy*
- ²⁹ *INFN Sezione di Genova, Genova, Italy*
- ³⁰ *INFN Sezione di Milano, Milano, Italy*
- ³¹ *INFN Sezione di Milano-Bicocca, Milano, Italy*
- ³² *INFN Sezione di Cagliari, Monserrato, Italy*
- ³³ *INFN Sezione di Padova, Padova, Italy*
- ³⁴ *INFN Sezione di Perugia, Perugia, Italy*
- ³⁵ *INFN Sezione di Pisa, Pisa, Italy*
- ³⁶ *INFN Sezione di Roma La Sapienza, Roma, Italy*
- ³⁷ *INFN Sezione di Roma Tor Vergata, Roma, Italy*
- ³⁸ *Nikhef National Institute for Subatomic Physics, Amsterdam, Netherlands*
- ³⁹ *Nikhef National Institute for Subatomic Physics and VU University Amsterdam, Amsterdam, Netherlands*
- ⁴⁰ *AGH - University of Krakow, Faculty of Physics and Applied Computer Science, Kraków, Poland*
- ⁴¹ *Henryk Niewodniczanski Institute of Nuclear Physics Polish Academy of Sciences, Kraków, Poland*
- ⁴² *National Center for Nuclear Research (NCBJ), Warsaw, Poland*
- ⁴³ *Horia Hulubei National Institute of Physics and Nuclear Engineering, Bucharest-Magurele, Romania*
- ⁴⁴ *Affiliated with an institute covered by a cooperation agreement with CERN*
- ⁴⁵ *DS4DS, La Salle, Universitat Ramon Llull, Barcelona, Spain*
- ⁴⁶ *ICCUB, Universitat de Barcelona, Barcelona, Spain*
- ⁴⁷ *Instituto Galego de Física de Altas Enerxías (IGFAE), Universidade de Santiago de Compostela, Santiago de Compostela, Spain*
- ⁴⁸ *Instituto de Física Corpuscular, Centro Mixto Universidad de Valencia - CSIC, Valencia, Spain*
- ⁴⁹ *European Organization for Nuclear Research (CERN), Geneva, Switzerland*
- ⁵⁰ *Institute of Physics, Ecole Polytechnique Fédérale de Lausanne (EPFL), Lausanne, Switzerland*
- ⁵¹ *Physik-Institut, Universität Zürich, Zürich, Switzerland*
- ⁵² *NSC Kharkiv Institute of Physics and Technology (NSC KIPT), Kharkiv, Ukraine*
- ⁵³ *Institute for Nuclear Research of the National Academy of Sciences (KINR), Kyiv, Ukraine*
- ⁵⁴ *School of Physics and Astronomy, University of Birmingham, Birmingham, United Kingdom*
- ⁵⁵ *H.H. Wills Physics Laboratory, University of Bristol, Bristol, United Kingdom*
- ⁵⁶ *Cavendish Laboratory, University of Cambridge, Cambridge, United Kingdom*
- ⁵⁷ *Department of Physics, University of Warwick, Coventry, United Kingdom*
- ⁵⁸ *STFC Rutherford Appleton Laboratory, Didcot, United Kingdom*
- ⁵⁹ *School of Physics and Astronomy, University of Edinburgh, Edinburgh, United Kingdom*
- ⁶⁰ *School of Physics and Astronomy, University of Glasgow, Glasgow, United Kingdom*
- ⁶¹ *Oliver Lodge Laboratory, University of Liverpool, Liverpool, United Kingdom*
- ⁶² *Imperial College London, London, United Kingdom*
- ⁶³ *Department of Physics and Astronomy, University of Manchester, Manchester, United Kingdom*
- ⁶⁴ *Department of Physics, University of Oxford, Oxford, United Kingdom*
- ⁶⁵ *Massachusetts Institute of Technology, Cambridge, MA, United States*
- ⁶⁶ *University of Cincinnati, Cincinnati, OH, United States*
- ⁶⁷ *University of Maryland, College Park, MD, United States*
- ⁶⁸ *Los Alamos National Laboratory (LANL), Los Alamos, NM, United States*
- ⁶⁹ *Syracuse University, Syracuse, NY, United States*
- ⁷⁰ *Pontifícia Universidade Católica do Rio de Janeiro (PUC-Rio), Rio de Janeiro, Brazil, associated to ³*
- ⁷¹ *School of Physics and Electronics, Hunan University, Changsha City, China, associated to ⁸*
- ⁷² *Guangdong Provincial Key Laboratory of Nuclear Science, Guangdong-Hong Kong Joint Laboratory of Quantum Matter, Institute of Quantum Matter, South China Normal University, Guangzhou, China, associated to ⁴*
- ⁷³ *Lanzhou University, Lanzhou, China, associated to ⁵*

- ⁷⁴ *School of Physics and Technology, Wuhan University, Wuhan, China, associated to* ⁴
⁷⁵ *Departamento de Física , Universidad Nacional de Colombia, Bogota, Colombia, associated to* ¹⁶
⁷⁶ *Ruhr Universitaet Bochum, Fakultaet f. Physik und Astronomie, Bochum, Germany, associated to* ¹⁹
⁷⁷ *Eotvos Lorand University, Budapest, Hungary, associated to* ⁴⁹
⁷⁸ *Van Swinderen Institute, University of Groningen, Groningen, Netherlands, associated to* ³⁸
⁷⁹ *Universiteit Maastricht, Maastricht, Netherlands, associated to* ³⁸
⁸⁰ *Tadeusz Kosciuszko Cracow University of Technology, Cracow, Poland, associated to* ⁴¹
⁸¹ *Universidade da Coruña, A Coruña, Spain, associated to* ⁴⁵
⁸² *Department of Physics and Astronomy, Uppsala University, Uppsala, Sweden, associated to* ⁶⁰
⁸³ *University of Michigan, Ann Arbor, MI, United States, associated to* ⁶⁹

^a *Centro Federal de Educacão Tecnológica Celso Suckow da Fonseca, Rio De Janeiro, Brazil*

^b *Center for High Energy Physics, Tsinghua University, Beijing, China*

^c *Hangzhou Institute for Advanced Study, UCAS, Hangzhou, China*

^d *School of Physics and Electronics, Henan University , Kaifeng, China*

^e *LIP6, Sorbonne Université, Paris, France*

^f *Lamarr Institute for Machine Learning and Artificial Intelligence, Dortmund, Germany*

^g *Universidad Nacional Autónoma de Honduras, Tegucigalpa, Honduras*

^h *Università di Bari, Bari, Italy*

ⁱ *Università di Bergamo, Bergamo, Italy*

^j *Università di Bologna, Bologna, Italy*

^k *Università di Cagliari, Cagliari, Italy*

^l *Università di Ferrara, Ferrara, Italy*

^m *Università di Genova, Genova, Italy*

ⁿ *Università degli Studi di Milano, Milano, Italy*

^o *Università degli Studi di Milano-Bicocca, Milano, Italy*

^p *Università di Padova, Padova, Italy*

^q *Università di Perugia, Perugia, Italy*

^r *Scuola Normale Superiore, Pisa, Italy*

^s *Università di Pisa, Pisa, Italy*

^t *Università della Basilicata, Potenza, Italy*

^u *Università di Roma Tor Vergata, Roma, Italy*

^v *Università di Siena, Siena, Italy*

^w *Università di Urbino, Urbino, Italy*

^x *Universidad de Alcalá, Alcalá de Henares , Spain*

^y *Facultad de Ciencias Físicas, Madrid, Spain*

^z *Department of Physics/Division of Particle Physics, Lund, Sweden*

[†] *Deceased*